Two-phase free jet model of an atmospheric entrained flow gasifier

Christian Hotz[a], Manuel Haas[a], Simon Wachter[a], Sabine Fleck[a], Thomas Kolb[a,b]

[a] Karlsruhe Institute of Technology (KIT), Institute for Technical Chemistry, Gasification Technology Department (ITC), Hermann-von-Helmholtz-Platz 1, 76344 Eggenstein-Leopoldshafen, Germany

[b] Karlsruhe Institute of Technology (KIT), Engler-Bunte-Institute, Division of Fuel Technology (EBI ceb), Engler-Bunte-Ring 1, 76131 Karlsruhe, Germany

Corresponding author: Christian Hotz, christian.hotz@partner.kit.edu

Abstract

We present a steady-state two-phase fluid dynamic model based on a classical free jet approach for the simulation of the main reaction zone in an atmospheric entrained flow gasifier. Radial Gaußian profiles of the mixing ratio and velocity for single-phase free jets taken from literature are adapted to the two-phase free jet. Exchange of momentum and mass between the jet and the surrounding is described by a parameter derived from atomization experiments under ambient conditions. With the free jet equations, a pattern of gas phase velocity and temperature is calculated. Droplets are introduced at the nozzle, accelerated, heated up and evaporated. Initial droplet size fractions are measured under ambient conditions. Sub-process models for fuel decomposition, oxidation and the water gas shift reaction are included in the model. The interaction of the sub-process models and the free jet equations are considered via balance equations for momentum, mass and enthalpy, solved in each control volume. The two-phase free jet model (2Ph-FJM) calculates the local composition, velocity and temperature of the gas phase as well as velocity, temperature and evaporation of the fuel droplet fractions. Simulation results are approved for a set of experimental data (i.e. droplet velocity, droplet size distribution and flame structure via OH*-chemiluminescence imaging) from the bench-scale atmospheric entrained flow gasifier REGA.

Keywords: two-phase free jet, fluid dynamic modeling, entrained flow gasification, flame structure, phase Doppler anemometry, OH*-chemiluminescence

1 Introduction

KIT operates the bioliq® plant with a 5 MW entrained flow gasifier as the central component of the process chain to convert biogenic and anthropogenic residues to synthesis gas for production of fuels and base chemicals. Supporting research on entrained flow gasification is carried out in a bench scale 60 kW Research Entrained Flow Gasifier (REGA) [1]. An overview of sub-processes relevant for the entrained flow gasification process is given in [1]. The objective of the present paper is to create and validate a computational model for the simulation of the two-phase flow in the main reaction zone of an entrained flow gasifier. Temperature, main gas components and velocity pattern of the gas phase as well as velocity, heat up and evaporation of the fuel droplet fractions are to be described. The model is to be used to perform sensitivity studies on the influence of single model parameters (e.g. burner nozzle dimension, spray droplet size, operating conditions) and sub-process models (e.g.

evaporation of fuel droplets) on the gasification process (e.g. flame structure, fuel conversion).

In computational fluid dynamics, the area of interest is divided into discrete control volumes. Mass, momentum and energy transfer is balanced at the boundaries of the control volumes. In order to take turbulent mixing into account, turbulence models such as (k-ε)-model for Reynolds-averaged Navier–Stokes simulations (RANS) [2] or sub-grid turbulence models for large-eddy simulations (LES) [3] are implied. RANS and LES simulation give detailed data on local velocity, temperature and concentration, but these models are characterized by high demand of CPU time. The implementation of detailed sub-process models as well as iterative solver methods are time consuming. These powerful numerical simulation tool are thus not very suitable for sensitivity analysis. The two-phase free jet model (2Ph-FJM) presented in this paper is able to calculate the pattern of the main gas components, temperature and fuel conversion in the main reaction zone. Compared to RANS or LES simulation, CPU time required for the simulation is several orders of magnitude lower. Furthermore, the 2Ph-FJM has a modular structure, thus sub-process models can be changed. These features allow the performance of sensitivity studies in order to investigate the influence of single process parameters or sub-process models on the gasification process.

2 Methods

2.1 Description of the modeling case

Gasification experiments are carried out in the atmospheric Research Entrained Flow Gasifier (REGA) (see Figure 1, left). The reactor is fed with mono ethylene glycol (MEG) as a well-defined surrogate fuel for biogenic pyrolysis oils and with oxygen-enriched air as the gasification medium. The burner is a twin-fluid external mixing atomizer with a central fuel orifice and an annular gas gap (see Figure 1, right). The gasification medium is utilized as atomization medium as well. Droplet size and adiabatic reactor temperature can be adjusted independently by altering the oxygen enrichment. The gasification medium emerges from the burner nozzle at high velocity. The high momentum disintegrates the liquid fuel into droplets and accelerates the latter. Fuel droplets and gasification medium form a two-phase jet emerging from the burner nozzle and penetrating into the hot syngas atmosphere of the reaction chamber. Hot syngas from the surrounding of the jet is entrained and mixed with jet media [4]. A supply of syngas from downstream of the flame zone compensates for the gas entrained into the jet, thus, the entrainment results in a large outer recirculation eddy (see Figure 1, middle). Inside the jet, a reactive two-phase mixture is formed by the liquid fuel droplets (FL), the gasification medium (GM) and the recirculated gas (RG) (= syngas) entrained into the jet. The oxygen from the gasification medium reacts predominantly with the hot syngas components from the recirculated gas. The fuel droplets need to heat up and evaporate prior to reaction with oxygen. The chemical reaction of oxygen from the gasification medium with syngas components from the recirculating gas results in an inverse diffusion flame, which is superimposed by the evaporation and conversion of the fuel vapor. As the input feed of oxygen is sub-stoichiometric at the nozzle, the fuel vapor is primarily converted in absence of molecular oxygen. Additional detailed information about the experimental set-up is presented in [1].

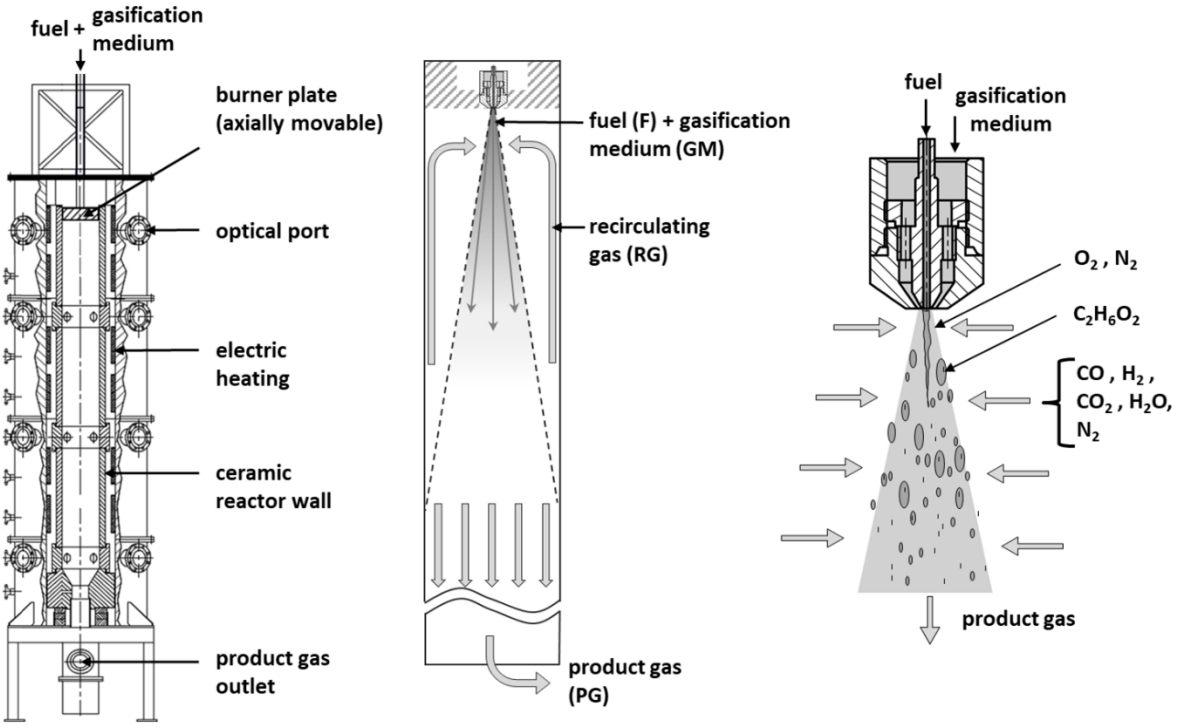

Figure 1: Overview of the modeling case with the experimental set-up of the entrained flow gasification experiments and the thermo-chemical processes taking place. Left side: Axial cut through the reactor of the REGA gasifier [1]. Middle: Scheme of the flow pattern inside the reactor with the main flows involved. Right side: Scheme of the near-burner zone [5].

2.2 Free jet theory

The two-phase free jet model (2Ph-FJM) is based on a classical turbulent free jet approach to describe the pattern of time-averaged velocity and concentration. The turbulent free jet is studied for many decades both analytically and experimentally. At the early outset of the investigation, Ruden [6] used a dynamic pressure probe to measure the mean velocity in a turbulent jet. In 1951, Reichardt [7] developed a model to describe the mean velocity in a turbulent jet. The development of hot wire anemometry allowed for the measurement of the turbulent structure of the free jet. Attempts to extend the classical free jet theory in order to describe the turbulent structure of the free jet have not been successful [8]. With the development of laser measuring techniques and gas chromatography, concentration profile in the jet could be measured [9,10]. Both measuring techniques and experimental set-up were further enhanced for decades. Experimental data obtained from Dowling (1990) [11], Panchapakesan (1993) [12] and Hussein et al. (1994) [13] are still used as benchmarks for the validation of computational fluid dynamics models.

Single-phase free jet without temperature / gas composition gradient

A single-phase free jet at ambient conditions without any gradient in temperature and gas composition emerges from the nozzle with the diameter d_0 (see Figure 2). The nozzle outlet velocity u_0 is constant in the core region, which ends at $z \approx 4 \cdot d_0$. Subsequent, after a transition region, the beginning of the self-similar region is located at a distance of approximately 6 - 8 nozzle diameters [11,14,15]. The onset of the self-similar region may be influenced by the initial outlet condition, the turbulence level and the nozzle design [16,17].

In the self-similar region, turbulent momentum exchange between the jet medium and the quiescent surrounding gas takes place, whereby gas from outside the jet entrains into the jet and mixes with jet medium. Thereby, the moving mass of the jet increases and the velocity decreases, with the overall momentum of the jet being conserved [13]. Due to the entrainment, the moving mass $\dot{m}_G$ increases linearly with the axial distance z to the nozzle taking into account a virtual jet point source at $z = z_0$ (eq. (1)) [4,18]. On the centerline of the jet, the velocity is reciprocally proportional to the axial distance $1/z$ (see eq. (2)). The centerline decay rate of the velocity $B_u \approx 5.9 - 6.1$ is obtained from experiments as a constant value for all turbulent single-phase free jets [12,13]. The radial velocity profiles of the jet are in good accordance with Gaußian curves [7,14,19–23]. Furthermore, radial velocity profiles collapse on a single line, when the profiles are normalized by the nozzle diameter, which is considered as self-similarity [12,13,24]. Taking these characteristics into account, Günther [25] and Kremer [26] developed an explicit equation to describe the velocity of a turbulent free jet at the axial distance z and the radial distance r (see eq. (3)). This equation contains a parameter for the exchange of momentum c_i, which is an empiric constant. Eq. (1) - (3) are only valid for a free jet without any gradient in temperature and gas composition between jet medium and surrounding.

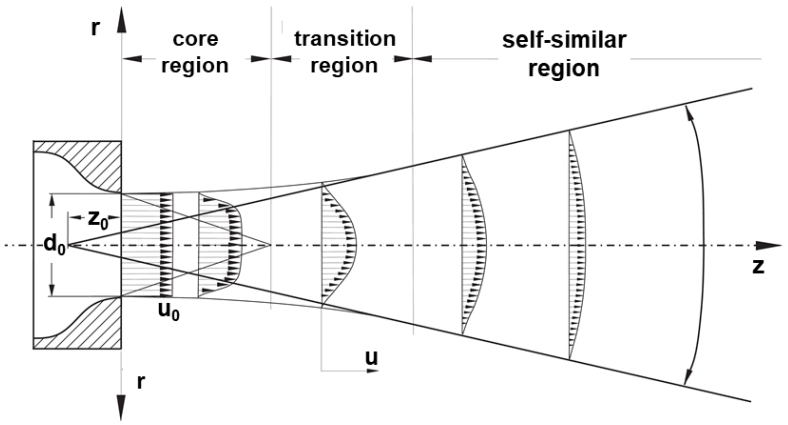

Figure 2: Radial velocity profiles of a free jet emerging from a nozzle, with the evolution of the three regions in a free jet [25,27].

$$\frac{\dot{m}_g(z)}{\dot{m}_{g,0}} = 0.32 \cdot \frac{z - z_0}{d_0} \tag{1}$$

$$\frac{u(z,0)}{u_0} = B_u \cdot \frac{d_0}{z - z_0} \tag{2}$$

$$\frac{u(r,z)}{u_0} = \frac{1}{2 \cdot c_i} \cdot \frac{d_0}{z - z_0} \cdot \exp\left(-\frac{1}{2 \cdot c_i^2} \cdot \left(\frac{r}{z - z_0}\right)^2\right) \tag{3}$$

Single-phase free jet with temperature / gas composition gradient

After a short distance downstream, the mass entrained into the jet exceeds the initial mass flow of the gas $\dot{m}_{g,0}$ emerging from the nozzle significantly (see eq. (1)). Therefore, the jet is characterized by the high entrainment rate and thus a high degree of dilution of the initial mass flow from the nozzle. In case of a density gradient between the medium from the nozzle and the surrounding due to a difference in temperature and / or the gas composition, the density of the jet asymptotically approaches the density of the surrounding. Considering this characteristic, Thring & Newby [28] introduced the concept of the equivalent nozzle diameter d_{eq}. d_{eq} is the diameter of the hypothetical jet with the same mass flow rate $\dot{m}_{g,0}$ and momentum flow rate $\dot{I}_0$ as the emerging jet, but calculated with the gas density of the surrounding ρ_1 (eq. (4)). Replacing d_0 by d_{eq} in eq. (1) - (3), the equations become valid for both the free jet with and without density gradient to the surrounding.

$$d_{eq} = \frac{2 \cdot \dot{m}_{g,0}}{\sqrt{\dot{I}_0 \cdot \pi \cdot \rho_1}} \tag{4}$$

A local mixing ratio is defined as the mass ratio of different flows (eq. (5)). A flow itself can consist of different molecular components (e.g. air). For a single phase free jet, the mixing ratio is the ratio of gas originating from the nozzle $m_{g,0}(z,r)$ and the gas entrained $m_{g,1}(z,r)$ (see left side of eq. (6)). For a non-reacting free jet, the mixing ratio is equivalent to a mass concentration. The mixing ratio of a free jet is reciprocally proportional to the axial distance (eq. (6). The centerline decay rate of the mixing ratio is $B_c \approx 4.6 - 5.1$ [11,15,29]. Analogous to the radial velocity profiles, the radial profiles of the concentration are also Gaußian shaped [7,14,19–23].

$$X_i = \frac{m_i}{\sum m_i} \tag{5}$$

$$X_0(z,0) = \frac{m_{g,0}(z\,,0)}{m_{g,0}(z\,,0) + m_{g,1}(z\,,0)} = B_c \cdot \frac{d_{eq}}{(z - z_0)} \tag{6}$$

Profiles measured at different axial distances z collapse on a single radial profile. Thus self-similarity is given [11,30–32] (see also Figure 6 left side in section 3.1). Even though, the gas from the nozzle is diluted due to entrainment, the overall mass flow of medium from the nozzle is conserved downstream, since gas is only entrained into the jet and not ejected out of the jet.

Summarizing, the turbulent single-phase free jet has the following characteristics:

- The momentum flow of the jet emerging from the nozzle is conserved downstream.
- The emerging jet medium is conserved downstream.
- The moving mass of the jet increases linearly with the axial distance from the nozzle.
- The centerline decay rate of velocity and concentration are constant.
- The radial profiles of velocity and the mixing ratio are self-similar.
- Radial profiles of velocity and the mixing ratio are Gauß-shaped.

Based on these six characteristics, Günther [25] and Kremer [26] developed explicit equations to describe the local velocity and mixing ratio in the self-similar region of a turbulent free jet (eq. (9) - (11)). The axial and radial position is expressed in a non-dimensional form (eq. (7) - (8)). Eq. (3) already introduced the equation for the velocity profile of a free jet with dimensioned variables without density gradient. Eq. (9) - (11) is valid for a single-phase free jet with density gradient due to different temperature or concentration of medium from the nozzle and the surrounding. In eq. (9) - (11), two empirical constants are contained, which are the parameter for exchange of momentum c_i and mass c_c. The value of c_i = 0.07 is obtained from experiments [26]. The value of c_c is derived from eq. (12), with the turbulent Schmidt number Sc_t set to 0.75 [25]. The velocity and the mixing ratio in the core region is equivalent to the flow at the nozzle (eq. (10), (13)). The transition region between core and self-similar region is not considered in the model.

Radial position:

$$\eta = \frac{r}{z - z_0} \tag{7}$$

Axial position:

$$\zeta = \frac{z - z_0}{d_{eq}} \tag{8}$$

Velocity in the self-similar region of a single-phase free jet:

$$u(\zeta, \eta) = \frac{u_0}{2 \cdot c_i \cdot \zeta} \cdot exp\left(-\frac{1}{2 \cdot c_i^2} \cdot \eta^2\right) \tag{9}$$

Velocity in the core region of a single-phase free jet:

$$u(\zeta, \eta) = u_0 \tag{10}$$

Mixing ratio in the self-similar region of a single-phase free jet:

$$\frac{m_{g,0}(\zeta, \eta)}{m_{g,0}(\zeta, \eta) + m_{g,1}(\zeta, \eta)} = \frac{Sc_t}{2 \cdot c_i} \cdot \frac{1}{\zeta} \cdot \exp\left(-\left(\frac{2 \cdot Sc_t - 1}{2 \cdot c_i^2}\right) \cdot \eta^2\right) \tag{11}$$

Definition of the turbulent Schmidt number [31]:

$$Sc_t = \frac{c_i^2}{c_c^2} \tag{12}$$

Mixing ratio in the core region of a single-phase free jet:

$$\frac{m_{g,0}(\zeta, \eta)}{m_{g,0}(\zeta, \eta) + m_{g,1}(\zeta, \eta)} = 1 \tag{13}$$

Two-phase free jet

The 2Ph-FJM is based on the single-phase free jet approach described above. In literature, the influence of a disperse phase on a gas phase of a free jet is discussed controversially. In particular, particles and droplets may influence the turbulence structure of a gas phase, i.e. alter entrainment and thus velocity and mixing ratio profiles in the free jet. Large droplets and particles may enhance turbulence due to the vortex shedding phenomena and intensify entrainment [33,34]. Small droplets and particles tend to have little effect or slightly decrease the levels of turbulence [34–36]. Two-phase free jets receive marginal attention in literature, which is mirrored also in a lack of systematic and detailed measurements [37]. To our knowledge, the description of a two-phase flow based on a free jet model is not available.

Confined jet

The reactor wall of the entrained flow gasifier encloses the jet, thus the total flow field in the reactor shows a jet in a confinement with the typical outer recirculation zone (see Figure 1, middle). Thring & Newby [28] developed a similarity parameter to describe the outer recirculation for confined jets. Applying the equivalent nozzle diameter, the theory is modified for non-isothermal jets [38]. For small values of the Craya-Curtet number C_t [39–41], which is typical for a jet emerging from a small nozzle compared to the reactor diameter, the position of the outer recirculation eddy can be calculated in good approximation by the modified Thring-Newby theory [41,42]. Thring-Newby showed that a confined jet can be described as a free jet up to the axial distance from the nozzle where the center of the outer recirculation eddy is located. Further downstream the jet is influenced by the outer recirculation. Between the center and the end of the recirculation eddy the free jet model loses its validity [43]. Following the Thring-Newby theory, the axial position of the center of the outer recirculation eddy is at $z = 0.44\ m$ for the geometry of the REGA gasifier and nozzle conditions applied. The end of the recirculation eddy is located at $z = 0.88\ m$.

2.3 The two-phase free jet model (2Ph-FJM)

2.3.1 Modeling concept

In the 2Ph-FJM, the jet is divided into control volumes (see Figure 3). In the present work, each control volume is 1.6 mm high and covers an angle of 0.12°. The simulated area is divided into 2800 equidistant slices in axial direction and 1000 slices in radial direction. The jet flow is assumed rotationally symmetric, thus only half of the control volumes in radial direction is calculated. The overall area simulated is a cone with the tip placed at the nozzle orifice.

In Figure 4, a schematic diagram of the 2Ph-FJM computational sequence is depicted. The computational sequence is divided into three sections. Section A contains the explicit free jet equations ($f(\zeta, \eta)$) taken from literature [25,26] for single-phase free jets. The free jet equations are adapted to the gas phase of the two-phase free jet with the parameter for exchange of momentum determined in atomization experiments (see section 3.1), which is representative for the spreading angle of the gas phase of the free jet.

In Section B of Figure 4, temperature and velocity of the gas phase in the two-phase flow is calculated based on two-phase balance equations solved in each control volume (ζ, η). The mixing ratio is calculated with the mass flows involved in the 2Ph-FJM: gasification medium

(GM), recirculated gas (RG) and overall mass of fuel (F), which is partly present as fuel vapor (FV) and partly present as liquid fuel (FL). The definition of the mixing ratio is given in eq. (14). The flow scheme is schematically depicted in Figure 1. The mixing ratio is determined from three known ratios. The local ratio of gasification medium and syngas entrained are calculated with the mixing ratio of the free jet calculated in Section A. The mass ratio of fuel and gasification medium is constant for each control volume, this mass ratio is equivalent to GLR (see eq. (34)), as it is assumed that the mass, that origins from the fuel droplets and the gasification medium do not segregate during atomization, evaporation or reaction. Therefore, the spray angle of the liquid is assumed to be equal to the spreading angle of the gas phase. The local ratio of fuel evaporated is calculated from the local droplet sizes. In a first iteration, the local droplet size is equal to the initial droplet sizes. Equations for the calculation of the mixing ratio are given in section 2.3.6.

Definition of the local mixing ratio in the 2Ph-FJM

$$X_i(\zeta\,,\eta) = \frac{m_i(\zeta\,,\eta)}{\sum m_i(\zeta\,,\eta)} \quad with\ \ i = GM, RG, FV, FL \tag{14}$$

In each control volume, a CSTR (continuous stirred-tank reactor) is considered. In a two-phase enthalpy balance, chemically bounded energy is transformed to heat. Heat transferred to the droplets for heating up and evaporation is taken into account. The gas phase (GM, RG, FV) reacts to chemical equilibrium. In a first iteration, local droplet temperatures and sizes is equal to the initial droplet temperatures and sizes. The reaction model results in the local gas phase temperature and molecular composition. The chemical reaction model utilized in the 2Ph-FJM is described in section 2.3.4.

On the right side of the middle section in Figure 4, the gas phase velocity is calculated, which is based on the free jet equation for velocity. Reaction induced acceleration of the gas phase is considered, thus the gas phase temperature is required (see section 2.3.5). In the two-phase momentum balance, the velocity of the reacting gas free jet is reduced by the momentum, which is transferred to the droplets. The gas phase (GM, RG, FV) has a common gas phase velocity. The velocities of the droplet fractions is calculated in the droplet model. In a first iteration, local droplet fraction velocities are equal to the initial droplet velocity (≈ 1 m/s).

In Section C of Figure 4, the droplet model is included. The droplets emerge from the nozzle and are transported through the pattern of the gas phase velocity and temperature, calculated in the middle section of Figure 4. Droplets are accelerated, heated up and evaporated. The kinetic sub-models for these processes are taken from literature (see section 2.3.2 and 2.3.3). Computation is performed for each droplet size fraction on each droplet pathway η from $\zeta = 0$ until the droplet is completely evaporated (see also Figure 3). Droplet velocities, temperatures and sizes are input parameter to the models in the middle section in Figure 4, thus an iterative calculation is executed. Iteration is terminated as change in local gas phase temperature is below 1K. In the following sections, sub-process models and balance equations for momentum and enthalpy utilized in the 2Ph-FJM are described.

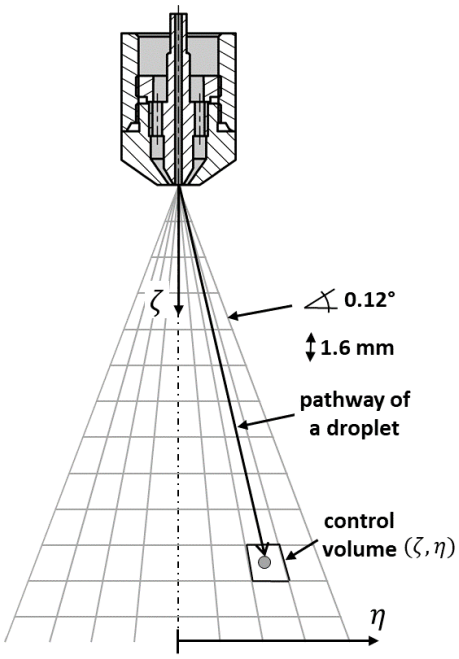

Figure 3: The structure of the control volumes and the pathways of droplets moving in the 2Ph-FJM.

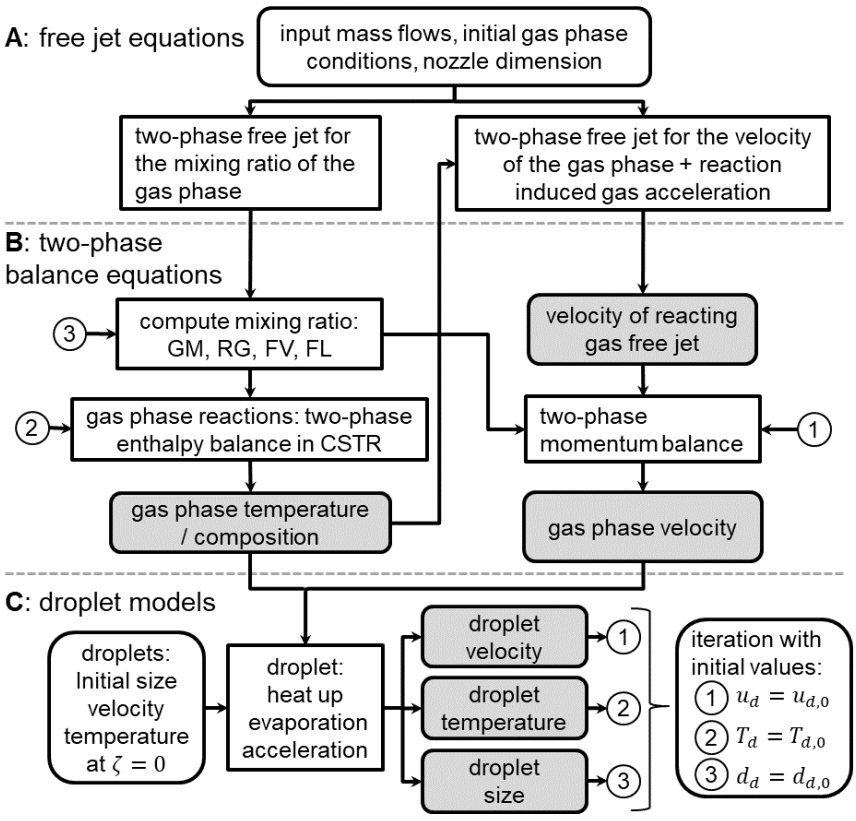

Figure 4: Computational sequence in the two-phase free jet model (2Ph-FJM).

2.3.2 Acceleration of fuel droplets

The liquid fuel of the entrained flow gasifier emerges from the central nozzle orifice at a typical velocity of $u_{0,FL} < 1\ m/s$. Gasification medium, emerging from the annular gap of the nozzle at high velocity, disintegrates the fuel and forms a poly-disperse droplet collective. Droplet size distribution is an input parameter to the model, which is taken from spray measurements using phase Doppler anemometry (see section 2.4.1).

The fuel droplets are accelerated in the jet. The acceleration rate of a droplet fraction $du_{d,k}/dt$ is derived from a force balance of the inertia force and the drag force of the droplet (eq. (15)) [44]. The drag coefficient $c_{D,k}$ is a function of the Reynolds number $Re_{d,k}$ (see eq. (16)), given in eq. (17) with coefficients given in Table 1 [45]. The correlation shows good performance on the relevant range of Reynolds numbers ($0 < Re_{d,k} < 1200$) of this work. Gravitational and buoyancy forces are neglected.

$$\frac{du_{d,k}}{dt} = \frac{6 \cdot c_{D,k} \cdot \rho_g}{8 \cdot d_{d,k} \cdot \rho_{d,k}} \cdot \left(u_g - u_{d,k}\right) \cdot \left|u_g - u_{d,k}\right| \tag{15}$$

$$Re_{d,k} = \frac{\left(u_{d,k} - u_g\right) \cdot \rho_g \cdot d_{d,k}}{\eta_g} \tag{16}$$

$$c_{D,k} = a_1 + \frac{a_2}{Re_{d,k}} + \frac{a_3}{Re_{d,k}^2} \tag{17}$$

Table 1: Coefficients of eq. (17) for modeling drag coefficient and corresponding Reynolds number for spherical smooth particles and droplets. [45]

a_1	a_2	a_3	$\mathrm{Re_d}$
0	24	0	$0 < \mathrm{Re_d} < 0.1$
3.69	22.73	0.0903	$0.1 < \mathrm{Re_d} < 1$
1.222	29.1667	-3.8889	$1 < \mathrm{Re_d} < 10$
0.6167	46.50	-116.67	$10 < \mathrm{Re_d} < 100$
0.3644	98.33	-2778	$100 < \mathrm{Re_d} < 1000$
0.357	148.62	-47500	$1000 < \mathrm{Re_d} < 5000$
0.46	-490.546	578700	$5000 < \mathrm{Re_d} < 10000$
0.5111	-1662.5	5416700	$\mathrm{Re_d} > 10000$

2.3.3 Heat up and evaporation of droplets

Heat up and evaporation is calculated consecutively within the model. The heat up model is based on the enthalpy balance for a droplet. The change of the droplet enthalpy (left side of eq. (18)) is equal to the heat flow rate to the droplet (right side of eq. (18)), with the mass of the droplet fraction $m_{d,k}$ and the heat capacity of the liquid $c_{p,d,k}$ [46]. Droplet temperature $T_{d,k}$ is assumed uniform across the droplet radius. The heat transfer coefficient α_k is obtained from a Nusselt correlation with a Ranz-Marshall approach given in eq. (19) - (20) [47]. In the

heat up model, only convective heat transfer is taken into account, radiative heat transfer is not considered.

$$m_{d,k} \cdot c_{p,d,k} \frac{dT_{d,k}}{dt} = \pi \cdot d_{d,k}^2 \cdot \alpha_k \cdot (T_g - T_{d,k}) \tag{18}$$

$$Nu_k = \alpha_k \cdot d_{d_k} / \lambda_g \tag{19}$$

$$Nu_k = 2 + 0{,}6 \cdot Re_{d_k}^{\frac{1}{2}} \cdot Pr^{\frac{1}{3}} \tag{20}$$

The evaporation model is based on the d^2-law, given in eq. (21), with the heat conductivity of the gas phase λ_g, density of the liquid droplet fraction ρ_{d_k} and heat capacity of the fuel vapor $c_{p,v}$ [47]. The equation is derived from an energy balance for an isothermal droplet. The mass transfer number $B_{T,k}$ is given in eq. (22) with the evaporation enthalpy h_v and the evaporation rate of the droplet fraction $\dot{m}_{v,k}$ given in eq. (23) [47]. Evaporation only starts, when the fuel droplet is heated up to the boiling point. This will overestimate evaporation time, since evaporation already takes place during heat up. However, evaporation actually takes place at the equilibrium evaporation temperature (wet bulb temperature), which is typically slightly below the boiling temperature of the liquid.

$$\frac{d d_{d_k}^2}{dt} = -\frac{8 \cdot \lambda_g \cdot \ln(1 + B_{T,k})}{\rho_{d_k} \cdot c_{p,v,k}} \tag{21}$$

$$B_{T,k} \equiv \frac{c_{p,v,k} \cdot \left(T_g - T_{d,k}\right)}{h_{v,k} + \dot{Q}_{d,k} / \dot{m}_{v,k}} \tag{22}$$

$$\dot{m}_{v,k} = \frac{2\pi \cdot d_{d,k} \cdot \lambda_g}{c_{p,v,k}} \cdot \ln\left(1 + B_{T,k}\right) \tag{23}$$

2.3.4 Chemical reaction model

Typical gas phase temperature in the main reaction zone is above 1800 °C, thus homogenous reactions are fast compared to the turbulent mixing process. Therefore, we assume infinite reaction rates or rather chemical equilibrium. The formation of by-products (e.g. soot, hydrocarbons) is not considered. For entrained flow gasification, this is mainly a small amount of typically < 1 vol.-% methane [48], which is not of relevance for the modeling prediction.

In our modeling case, monoethylene glycol ($C_2H_6O_2$) is utilized as a fuel. In the 2Ph-FJM, the fuel vapor is thermally decomposed to carbon monoxide and hydrogen (eq. (24). The product gas of the decomposition process is mixed with the gasification medium and the syngas entrained into the jet. This gas mixture contains CO, H_2, CO_2, H_2O, O_2 and N_2. Oxygen reacts with hydrogen and carbon monoxide (eq. (25) - (26)). In control volumes with fuel lean mixtures, concentration of CO_2, H_2O, O_2 and N_2 is derived from the element balance. For fuel rich mixtures, gas concentration is based on the water gas shift equilibrium (eq. (27)). The

equilibrium coefficient is defined in eq. (28). $K_{P,WGS}(T)$ is calculated from chemical equilibrium using ASPEN®. Nitrogen is regarded as an inert substance.

$$C_2H_6O_2 \rightarrow 2\,CO + 3\,H_2 \tag{24}$$

$$H_2 + 0.5 \cdot O_2 \rightarrow H_2O \tag{25}$$

$$CO + 0.5 \cdot O_2 \rightarrow CO_2 \tag{26}$$

$$CO + H_2O \rightleftharpoons CO_2 + H_2 \tag{27}$$

$$K_{P,WGS}(T) = \frac{\tilde{y}_{CO_2} \cdot \tilde{y}_{H_2}}{\tilde{y}_{CO} \cdot \tilde{y}_{H_2O}} \tag{28}$$

2.3.5 Reaction induced thrust of the gas phase

Chemical reactions, especially the oxidation of syngas components entrained into the jet with the oxygen from the gasification medium (eq. (25) - (26)) do effect the velocity of the free jet. Since oxidation is exothermic, gas phase temperature rises significantly, which causes expansion of the reacting gas mixture and results in additional thrust of the jet. In the calculation of volume expansion, only oxidation of syngas is considered. The evaporation and reaction of fuel is neglected as both do not contribute to a major temperature change.

In the 2Ph-FJM, velocity is based on a classical free jet calculated with the Gaußian profiles shown in eq. (9) and taken from [25]. In order to take reaction induced thrust into account, an additional term (first bracket in eq. (32)) is introduced in eq. (9). In eq. (32), a maximum relative volume expansion rate in axial direction of the gas mixture ϵ_{max} and a local degree of oxygen conversion x_{O2} is present. ϵ_{max} is calculated from the gasification medium (GM) reacting in an isobaric CSTR with a stoichiometric amount of recirculated gas (RG) producing product gas (PG). Please note that GM, RG and PG are gas mixtures. The stoichiometric ratio of GM and RG has to be calculated. The educts enter the CSTR at the initial states (temperature, composition), which is not a function of space (see Table 4 in section 4.1). The volume of the PG is larger than the sum of GM and RG due to a change in the temperature and the number of molecules during the reaction (see eq. (25) + (26)). The volume V_i (i = GM, RG, PG) is assumed as an ideal gas (eq. (29)). In eq. (30), the maximum relative volume expansion rate in axial direction ϵ_{max} is calculated. In axial direction, only the third root of the maximum volume expansion is regarded to act as additional thrust for the jet. In eq. (31), the local degree of oxygen conversion x_{O2} is defined as the ratio of local oxygen concentration of the product gas (after reaction) $y_{O2,PG}\,(\zeta\,,\eta)$ and the local oxygen concentration calculated from non-reacting free jet. In eq. (32), the maximum expansion rate is combined with the degree of the local oxygen conversion, since the additional thrust is only generated when combustible gas components are oxidized.

$$V_i = \frac{n_i \cdot R \cdot T_i}{p} \qquad with\ i = PG, GM, RG \tag{29}$$

$$\epsilon_{max} = \sqrt[3]{\frac{V_{PG}}{V_{GM} + V_{RG}} - 1} \tag{30}$$

$$x_{O2}(\zeta, \eta) = \frac{y_{O2,PG}(\zeta, \eta)}{X_{GM}(\zeta, \eta) \cdot y_{O2,GM}} \tag{31}$$

$$u_{FJ}(\zeta, \eta) = \left(1 + \epsilon_{max} \cdot x_{O2}(\zeta, \eta)\right) \cdot \frac{u_0}{2 \cdot c_i^2 \cdot \zeta} \cdot \exp\left(-\frac{1}{2 \cdot c_i^2} \cdot \eta^2\right) \tag{32}$$

2.3.6 Balancing equations of the two-phase free jet model

In this section, the local temperature, molecular composition and velocity of the product gas (PG) is calculated. Therefore, the gas phase model (free jet approach), liquid phase models (acceleration, heat up, evaporation) and chemical reactions model are combined via enthalpy, element and momentum balance. In a first step, the local mixing ratio X_i of the four flows is calculated. The definition of the mixing ratio is given in eq. (14). In each control volume, a mixing ratio X_i of the four mass flows (gasification medium (GM), recirculated gas (RG), fuel vapor (FV), liquid fuel (FL)) is present (see also scheme in Figure 1), which is calculated with the system of equations (14) & (33) - (37).
The sum of the four $X_i(\zeta, \eta)$ (eq. (14)) is equal to one, which is the closing condition.
The ratio of gas originated from the nozzle (GM) and entrained from the surrounding (RG) in eq. (33) is determined from the free jet approach, which is already introduced in eq. (11). In the core region of the free jet, the ratio calculated with eq. (11) is above 1. In this case, the free jet equation is not valid and the ratio is set to 1 (eq. (13)).
The local ratio of gasification medium (GM) and fuel (F) in eq. (35) is assumed to be constant across the jet and equivalent to the gas-to-liquid ratio (GLR) of the input flows of fuel and gasification medium at the nozzle, given in eq. (34).
In the 2Ph-FJM, k droplets with the initial droplet sizes $d_{d,k,0}$ are considered. The droplet evaporation rate is calculated for each of the k droplet size fraction individually (see section 2.3.3). From the local size of each droplet fraction $d_{d,k}(\zeta, \eta)$, the ratio of fuel (F), which is still liquid (FL) is obtained from eq. (36). The sum of fuel vapor (FV) and liquid fuel (FL) is equivalent to the overall mass of fuel (F) (eq. (37)).

Local mixing ratio for gasification medium and recirculated gas entrained into the two-phase free jet:

$$\frac{m_{GM}(\zeta, \eta)}{m_{GM}(\zeta, \eta) + m_{RG}(\zeta, \eta)} = \frac{Sc_t}{2 \cdot c_i} \cdot \exp\left(-\left(\frac{2 \cdot Sc_t - 1}{2 \cdot c_i^2}\right) \cdot \eta^2\right) \tag{33}$$

Definition of the gas-to-liquid ratio:

$$GLR = \frac{\dot{m}_{g,0}}{\dot{m}_{l,0}} \tag{34}$$

Assumption for the local ratio of gasification medium and fuel:

$$\frac{m_{GM}(\zeta\,,\eta)}{m_F(\zeta\,,\eta)} = GLR \tag{35}$$

Local ratio of liquid fuel mass and overall fuel mass

$$\frac{m_{FL}(\zeta\,,\eta)}{m_F(\zeta\,,\eta)} = \frac{\sum_k d_{d,k}^3(\zeta\,,\eta)}{\sum_k d_{d,k,0}^3} \tag{36}$$

Fuel mass balance:

$$m_F(\zeta\,,\eta) = m_{FV}(\zeta\,,\eta) + m_{FL}(\zeta\,,\eta) \tag{37}$$

For the calculation of the local temperature and molecular composition of the product gas (PG), each control volume is treated as a CSTR. GM, RG, FV and FL are considered as the educts, which are initially present in the control volume according to the local mixing ratio of the gas phase X_i calculated from eq. (14) & (33) - (37). The enthalpy of each flow (GM, RG, FV, FL) is according to its enthalpy at the initial state, which includes the individual molecular composition and temperature, which is constant and not a function of space (see Table 4 in section 4 for instance). The gasification medium (GM) is a mixture of nitrogen and oxygen at ambient temperature. Fuel vapor (FV) and liquid fuel (FL) are liquid glycol at ambient temperature. The temperature of the recirculated gas (RG) is assumed to be equal to the reactor wall temperature. The composition of the recirculated gas is calculated from the chemical equilibrium at wall temperature of the input flow of fuel and gasification medium. The overall enthalpy and elements are conserved. The three gaseous flows (GM, RG, FV) are assumed to react to chemical equilibrium (see section 2.3.4) and the liquid droplet (FL) temperature is calculated in the droplet heat up and evaporation model (see section 2.3.3). In order to calculate the local molecular concentration $y_{n,PG}$ (6 unknowns), defined in eq. (39), and the temperature T_{PG} (1 unknown) of the product gas (PG), the element balance for H, C, N and O (4 equations), the enthalpy balance (eq. (38)) and the water gas shift equilibrium (eq. (28)) is calculated for the gas phase. The sum of $y_{n,PG}$ in eq. (39) is equal to one, which is the closing condition. This system of equations of seven unknowns and seven equations has to be solved iteratively.

Enthalpy balance

$$\sum_i X_i(\zeta,\eta)\cdot h_i(T_i) = \frac{\sum_n m_{n,PG}(\zeta,\eta)\cdot h_n(T_{PG}) + m_{FL}(\zeta,\eta)\cdot h_{FL}(T_d)}{\sum_n m_{n,PG}(\zeta,\eta) + m_{FL}(\zeta,\eta)} \tag{38}$$

Definition of gaseous composition

$$y_{n,PG}(\zeta\,,\eta) = \frac{m_{n,PG}(\zeta\,,\eta)}{\sum_n m_{n,PG}(\zeta\,,\eta)} \tag{39}$$

$with\ \ i = GM, RG, FV, FL\ ,\ \ n = CO, CO_2, H_2, H_2O, N_2, O_2.$

For the calculation of the local gas phase velocity $u_g(\zeta,\eta)$, the momentum balance eq. (40) has to be solved for each control volume. All parameters in eq. (40) except $u_{0,FL}$ are local parameters dependent on $(\zeta\,,\eta)$. The gas phase velocity is based on the velocity pattern of the free jet $u_{FJ}(\zeta,\eta)$, taking into account the reaction induced thrust of the gas phase (eq.

(32)). In the core region of the free jet, the velocity of the free jet calculated with eq. (32) is higher than the velocity at the nozzle. In this case, the free jet equation is not valid and the velocity is set to the velocity at the nozzle $u_{g,0}$ (eq. (10)). Momentum is transferred from the gas phase to the droplets, due to the acceleration of the droplets. The left side of the momentum balance (eq. (40)) represents the overall momentum locally available, which can be calculated from the hypothetical state with no momentum transferred between the phases. Thus, the mass fraction of the droplets X_{FL} as well as fuel vapor X_{FV} move at fuel inlet velocity $u_{0,FL}$, which is typically $1\ m/s$. The gasification medium X_{GM} and entrained gas X_{RG} moves at the local velocity u_{FJ} according to a free jet calculated with eq. (32). The free jet equation implies the conservation of momentum of GM and RG entrained into the jet. On the right side of eq. (40), the actual state is described, with momentum transfer between the two phases. The k droplet fractions move at the individual velocity calculated in the kinetic droplet model in eq. (15) - (17). The mean velocity of the liquid phase X_{FL} is the mass weighted droplet mean velocity $\bar{u}_{FL}$. The gas phase $(X_{GM} + X_{RG} + X_{FV})$ moves at a common local velocity u_g, which is calculated with eq. (40). Since gas phase velocity is an input to the kinetic droplet model, velocity of the gas phase u_g and velocity of the k droplet fractions $\bar{u}_{FL}$ are calculated iteratively.

$$(X_{FV} + X_{FL}) \cdot u_{0,FL} + (X_{GM} + X_{RG}) \cdot u_{FJ} = X_{FL} \cdot \bar{u}_{FL} + (X_{GM} + X_{RG} + X_{FV}) \cdot u_g \quad (40)$$

The sets of equations for momentum, molecular species and enthalpy balance combined with the kinetic models for droplets acceleration, heat up and evaporation and the chemical reaction model given in section 2.3 allows for the calculation of the overall gasification process. This includes molecular concentration, temperature and velocity of the gas phase as well as the local size, temperature and velocity of the fuel droplet fractions.

2.4 Measuring Techniques

2.4.1 Spray Characterization by Phase Doppler Anemometry

Spatially resolved measurement of droplet velocity and droplet size distribution are performed using phase Doppler anemometry (PDA). The PDA technique is applied in ATMO (see Figure 5 at section 3.1) to measure droplet size distribution as an input to the 2Ph-FJM and in the REGA gasifier for validation of the simulation results from the 2Ph-FJM. The PDA system applied is a FlowExplorer DPSS300 2D and SprayExplorer 2D by DANTEC Dynamics, which operates in forward scattering mode using a focal length of 1000 mm and an off-axis angle of $\varphi = 70°$ between laser and receiver. The laser wavelength is 561 nm with a beam diameter of 2.2 mm and a beam spacing of 40 mm. In order to reduce potential measurement errors, a slit with a length of 200 µm and an asymmetrical mask (Mask B) are utilized. A Bragg-cell operated at a frequency shift of 80 MHz is used to determine the flow direction. Under these specifications, the detectable droplet size ranges from 1 µm to 1374 µm. The PDA receiver settings are determined by a sensitivity study to improve detection of small droplets. A detailed description of the PDA measuring applied technique can be found in [49].

The PDA is mounted on a 2D-traverse system, which is capable to move the measuring volume of the PDA in both horizontal directions. Measurements presented in this work are recorded

at different axial positions at the center of the free jet. The center is detected by highest velocity and highest data rate at each axial position. Axial resolution is achieved by moving the burner from z = 30 mm to z = 250 mm. To assure a sufficient amount of detected droplets, the termination criteria for the measurement is set to 50 000 droplets measured and measurement time limited to 60 s. In the present work, only data with more than 5000 droplets locally detected are considered.

The software toolbox SprayCAT described in [50] is used for processing the PDA data. For each point, the droplet mean velocity and the Sauter mean diameter SMD is evaluated as a characteristic diameter of the droplet size distribution.

2.4.2 OH*-Chemiluminescence Imaging

The flame structure in the entrained flow gasification experiment is described using OH*-chemiluminescence imaging. By measuring OH*-chemiluminescence, zones of high reaction intensity and high temperature are detected. The measurements are conducted with an intensified camera system consisting of an image intensifier (LaVision IRO) equipped with an UV-objective (f = 85 mm) and a CMOS-camera (Imager M-Lite 2M, LaVision). Two bandpass filters (λ = 342 nm, 85 nm FWHM, LaVision, and λ = 357 nm, 48 nm FWHM, EdmundOptics) are used to measure OH*- and CO2*-chemiluminescence respectively. Since the broadband CO2*-chemiluminescence can make a major contribution to the total chemiluminescence, especially in syngas flames [51–53], the CO2*-contribution has to be subtracted from the OH*-filter image to reveal the actual OH*-chemiluminescence distribution. For this purpose, a method developed by Lauer et al. is applied [54–56].The spatial resolution of the camera is 0.2 mm per pixel. 200 images are recorded with a framerate of 50 Hz and a gate time of 10 ms. The optical access at the REGA test rig does not allow for a complete imaging of the entire flame in a single take. Thus, the burner is axially moved and single shots taken at different positions are merged in the post-processing. The resulting flame images are temporal averaged and processed with an inverse Abel-transformation.

3 Experimental determination of model input data

3.1 Determination of the parameter for exchange of momentum c_i for the 2Ph-FJM

The parameter for the exchange of momentum c_i for the calculation of local concentration profiles in the 2Ph-FJM are derived from experiments under ambient conditions in the Atmospheric Spray Test Rig (ATMO). The experimental set-up is shown in Figure 5. The nozzle utilized is a twin-fluid external mixing atomizer with a central orifice for the liquid and an annular gap for the gaseous atomization medium. The liquid is water, which is atomized with pressurized air. The local ratio of gas emerging from the nozzle $m_{G,0}$ and gas entrained from the surrounding m_{RG} is determined by concentration measurements. In order to distinguish atomization medium and air entrained from the surrounding, the pressurized air is enriched with helium as a tracer gas. Tracer gas concentration at the nozzle $y_{0,He}$ and local concentration in the jet $y_{He}(\zeta, \eta)$ is measured with a gas chromatography system. This method is adapted from [57,58]. The local ratio of the gas phase is determined from eq. (41). In order to determine the parameter for exchange of momentum c_i, the Gaußian

concentration profiles of the free jet in eq. (11) is fitted to measured concentration profiles using least square method, with the turbulent Schmidt number Sc_t = 0.75 [25].

$$\frac{m_{G,0}(\zeta,\eta)}{m_{G,0}(\zeta,\eta)+m_{RG}(\zeta,\eta)}=\frac{y_{He}(\zeta,\eta)}{y_{He,0}} \tag{41}$$

Operating conditions chosen are typical for gasification experiments conducted in the REGA gasifier. The mass flow of the gas phase $\dot{m}_{g,0}$ is shown in Table 2. The liquid mass flow $\dot{m}_{l,0}$ is varied according to a gas-to-liquid ratio GLR = 0.50 / 0.75 / 1.00 / 1.25 / 1.50, (see eq. (34)). The tracer gas concentration in the two-phase free jet is measured at normalized axial distance ζ = 10 / 15 / 20 / 30 / 50 and at normalized radial distance at 19 positions in the range of η = ±0.3.

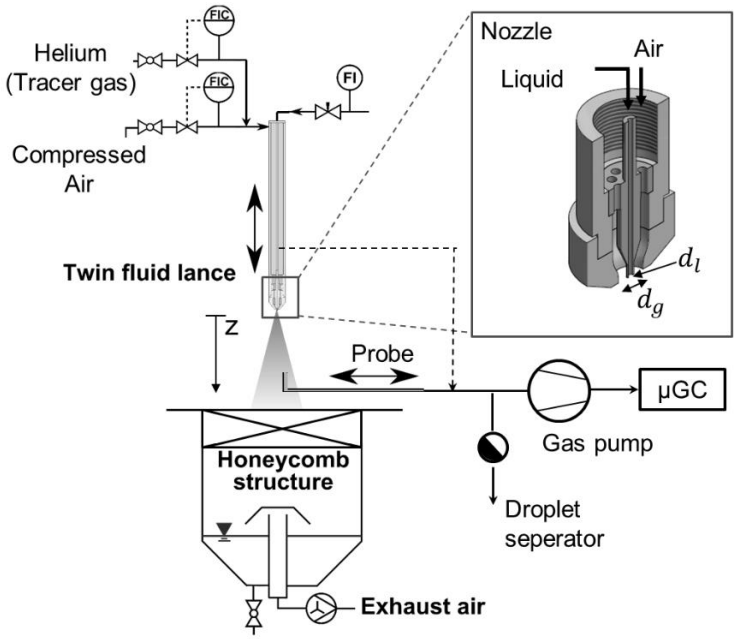

Figure 5: Experimental set-up of atmospheric spray test rig (ATMO) with gas probe for helium tracer gas.

Table 2: Nozzle dimensions and associated operating conditions of the gas phase

Parameter	Value
d_l / mm	2.0
d_g / mm	7.2
d_{eq} / mm	6.6
$\dot{m}_{g,0}$ / kg/h	10.0
$u_{g,0}$ / m/s	72
$\dot{I}_{g,0}$ / N	0.2
Re_g / 1000	20.4

The left side of Figure 6 depicts the measured values of tracer gas concentration. The parameter for exchange of momentum c_i is derived by fitting eq. (11) to the measured data

using least-square method. c_i is determined to 0.0884, which is used for modeling in the 2Ph-FJM. For the single-phase free jet, the parameter for exchange of momentum is constant ($c_i = 0.07$). We assume that the atomization process initiates the difference for c_i for the two-phase experiment. High-speed camera images show a periodical movement in radial direction of the liquid jet emerging from the central orifice (see Figure 6, right side). Following Chigier and Farago [59], the operating conditions can be classified as fiber-type atomization regime. In this atomization regime the occurrence of a flapping liquid jet caused by a Kevin-Helmholtz instability is typical. The radial acceleration of the droplets leading to a wide spray angle [60]. The radial movement of the droplets may also enhance radial mixing of the gas phase and therefore entrainment. This effect results in an increase of c_i. In experiments with operation conditions in super-pulsating atomization regime without flapping, c_i is determined close to 0.07, which is not part of this publication.

The experimental data, measured at different axial distance to the nozzle, collapse on a single radial profile. Thus, radial concentration profiles of the two-phase free jet show self-similarity. Since the model equation is based on a Gaußian profile, the two-phase free jet also shows Gaußian shape, which is in accordance to the single-phase free jet.

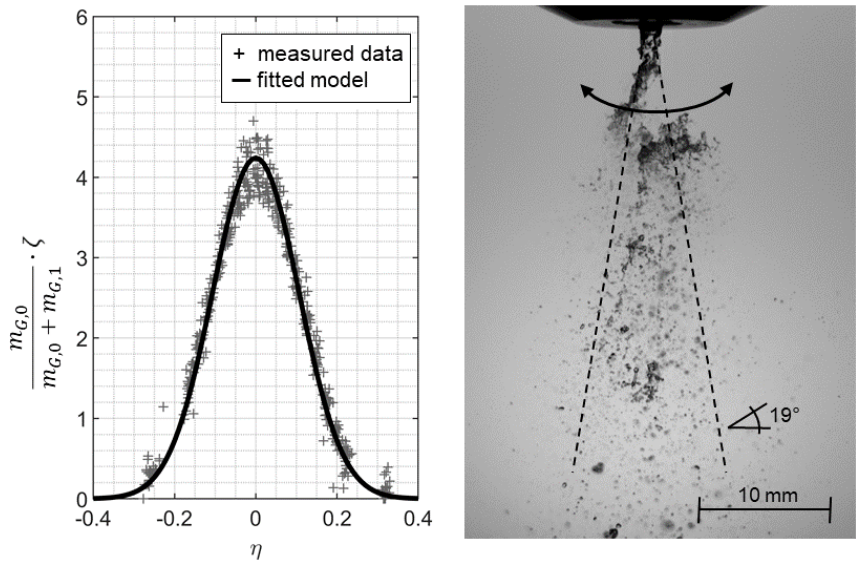

Figure 6: Left: Measured radial tracer gas concentration profiles presented in non-dimensional self-similar form and fitted eq. (11) for the determination of c_i. Right: High-speed camera images of the area near the nozzle orifice during atomization under ambient conditions in different atomization regimes. Camera setting according to [50].

3.2 Atomization

In the 2Ph-FJM, atomization is assumed to be completed at the nozzle outlet, thus spherical fuel droplets emerges from the nozzle. The initial droplet size distribution is determined from PDA experiments at the ATMO test rig measured at axial distance of z = 200 mm (see section 2.4.1). The atomization medium is pressurized air and the liquid is glycol. The mass flow of the liquid and the atomization medium are equivalent to the gasification experiments (see Table 3). Nozzle dimensions are given in Table 2. As initial droplet size fractions for the model, k droplet sizes are drawn from the local droplet size distribution Q_3 on the axis (see Figure 7).

Each droplet size fraction represents equal mass fraction of the overall fuel mass input flow. For this work, $k = 50$ droplet size fractions are used.

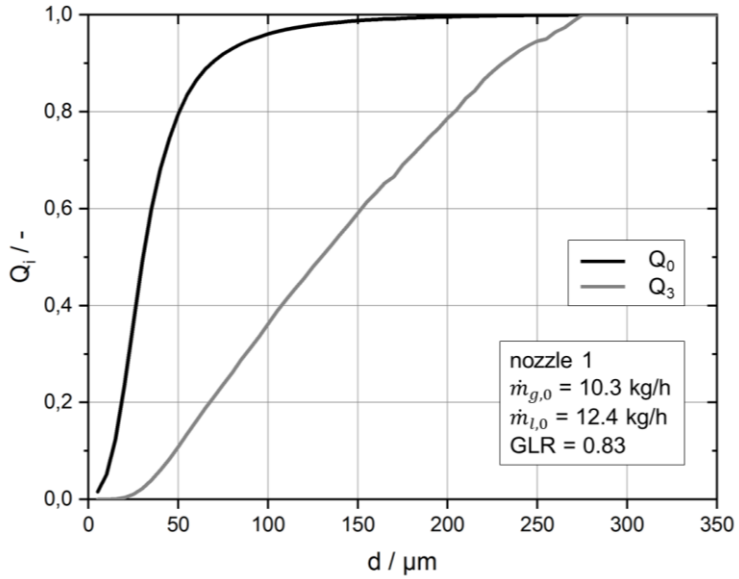

Figure 7: Initial drop size distribution Q_0 and Q_3 of the entrained flow gasification modeling case, measured with phase Doppler anemometry under ambient condition at z = 200 mm.

4 Results and discussion

4.1 Simulation results

The simulation of the entrained flow gasification is performed using the two-phase free jet model (2Ph-FJM). Monoethylene glycol is used as a liquid fuel and oxygen enriched air is used as gasification medium. The modeling case is described in detail in section 2.1. The nozzle dimensions are given in Table 2, with an equivalent nozzle diameter of d_{eq} = 17.6 mm (see eq. (4)). The input flows and velocities at the nozzle orifice of the fuel and gasification medium as well as the reactor wall temperature are given in Table 3.

Table 3: Operating conditions for the atmospheric entrained flow gasification experiments with monoethylene glycol as fuel and oxygen enriched air as the gasification (see section 3.1).

parameter	unit	value
$\dot{m}_{F,0}$	kg / h	12.4
$\dot{m}_{GM,0}$	kg / h	10.3
$u_{GM,0}$	m / s	68.7
$u_{F,0}$	m / s	0.99
T_{wall}	K	1473

Table 4: Temperature and composition of the three flows involved (fuel, gasification medium and recirculated gas).

	F	GM	RG
T / K	303	303	1473
$\tilde{y}_{CO}$	0	0	0.242
$\tilde{y}_{CO_2}$	0	0	0.121
$\tilde{y}_{H_2}$	0	0	0.244
$\tilde{y}_{H_2O}$	0	0	0.300
$\tilde{y}_{N_2}$	0	0.307	0.093
$\tilde{y}_{O_2}$	0	0.693	0
$\tilde{y}_{C_2H_6O_2}$	1	0	0

The simulation results of the 2Ph-FJM are shown below. Figure 8 depicts the gas temperature and Figure 9 shows corresponding radial profiles of gas temperature and composition at three axial positions. Close to the burner nozzle, a cold core is present in the central area of the jet (see Figure 8). Inside the core, oxygen from the gasification medium remains unreacted, since neither fuel is yet evaporated nor hot syngas is entrained. Here, temperature and composition of the gas phase is equal to gas inlet condition of the gasification medium (see also Figure 9, z = 50 mm).

Ignition and flame stabilization is location immediately at the nozzle exit, slightly displaced from the jet axis, where hot syngas from the surrounding entrains and mixes with the oxygen of the gasification medium from the nozzle. A rotational symmetric reaction zone is formed, enveloping the cold core. At the radial position, where stoichiometric condition is reached (see Figure 9, r ≈ 10 mm), temperature and concentration of oxidation products (H_2O, CO_2) show a distinct peak. However, temperature in this region is overestimated since both gas radiation and formation of radicals are not considered in the 2Ph-FJM. For r > 10 mm, the gas phase approaches the composition of the recirculating syngas asymptotically.

Close to the nozzle, radial profiles of temperature and concentration show steep gradients in the reaction zone. With increasing axial distance, the profiles flatten since entrainment of recirculated syngas into the jet proceeds. At z = 150 mm, only a small amount of oxygen remains on the jet axis. The major part of oxygen has reacted with syngas, leading to high temperature and high concentration of oxidation products. As the gas temperature increases, droplets evaporate significantly releasing combustible fuel vapor and contributes to the oxidation reaction. At an axial distance of z ≈ 160 mm, the rotationally symmetric reaction zone merges on the axis (see Figure 8). Further downstream, the gas composition falls below the stoichiometric ratio, due to the entrainment of recirculated syngas. Thus reaction intensity as well as peak temperature decays (see Figure 9, z = 250 mm).

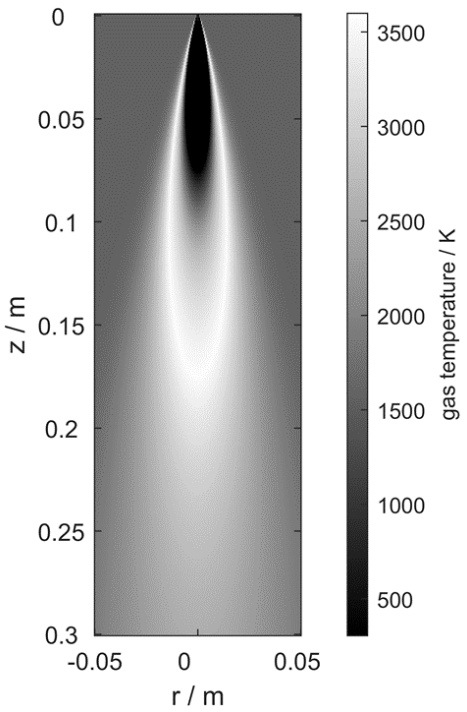

Figure 8: Gas phase temperature simulated with the 2Ph-FJM (d_{eq} = 17.6 mm).

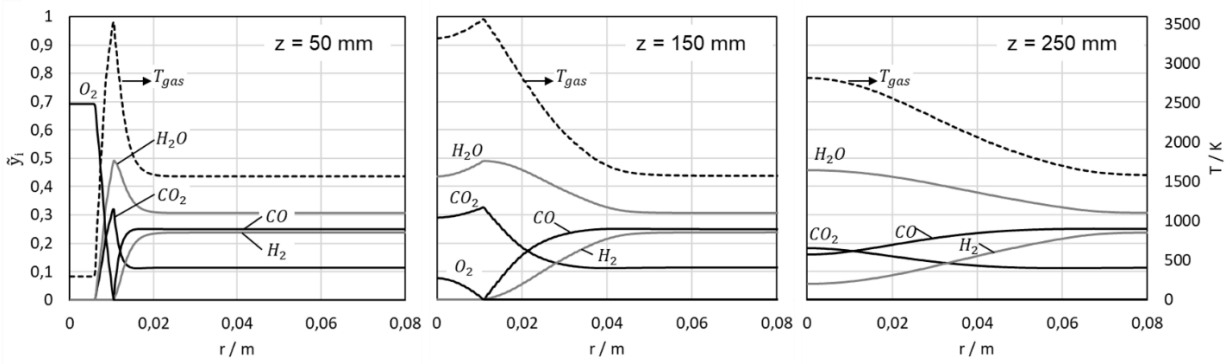

Figure 9: Radial profiles of gas phase temperature and composition at three different axial positions simulated with two-phase free jet model (d_{eq} = 17.6 mm).

In Figure 10, gas and droplet velocities on the flame axis are depicted. The core region of the free jet is located between 0 mm < z < 95 mm. The gas phase emerges from the nozzle orifice (z = 0) at a velocity of 69 m/s, the liquid phase emerges at a velocity of 1 m/s. Due to the momentum transfer from the gas phase to the droplets, the droplets are accelerated and the gas phase is decelerated. The acceleration of small droplets proceeds rapidly, whereas large droplets have high inertia and experience only moderate acceleration. Since number-averaged mean droplet velocity is dominated by small droplet fractions, the increase of the number-average droplet velocity is also rapid compared to the mass-averaged droplet velocity. Droplet acceleration can be observed in the area close to the nozzle (z < 50 mm), where velocity difference of the droplets and the gas phase is high. At z = 95 mm, the self-similar region starts and the gas phase is decelerated due to entrainment (see section 2.1), causing a first small hump in Figure 10. A transition zone between core zone and self-similar

region is not part of the 2Ph-FJM. In the range of 75 mm < z < 160 mm, the main reaction zone is located on the axis. The oxidation causes additional thrust, which accelerates the gas phase (see section 2.3.5). This zone smoothly starts at z ≈ 75 mm and ends abruptly as the oxygen is completely consumed at z = 160 mm. Since no additional thrust from reaction is available at z >160 mm, the gas phase decelerates, which can be seen in a second hump in Figure 10. In the range of 75 mm < z <160 mm, the additional thrust mostly compensates for the deceleration of the gas phase due to entrained gas, which starts at z = 95 mm, thus a plateau of the gas velocity is present.

As the gas phase velocity drops below the velocity of a droplet size fraction, the droplet velocity decelerates and momentum is transferred from the droplet to the gas phase. After a distance of z ≈ 350 mm, velocity of the gas is below the slowest droplet fraction, thus velocity of all droplet size fractions decreases. During the lifetime of a droplet fraction, inertia of the droplet decreases due to the evaporation. As the droplet fraction is completely evaporated, the droplet fraction velocity equals the gas phase velocity.

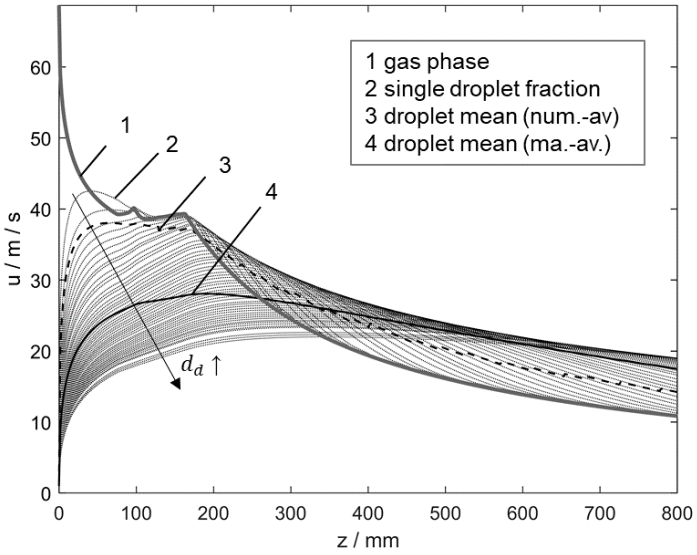

Figure 10: Velocity in the entrained flow gasifier on the flame axis (r = 0) simulated with the 2Ph-FJM. Gas phase velocity, single droplet fraction velocities, mass-averaged and number averaged mean droplet velocity.

In the present work, 2.8 million control volumes und 50 droplet size fractions are considered. Time required for simulation is in the order of a few hours using a single processor core. Compared to RANS or LES simulation, CPU time required for the simulation is several orders of magnitude lower. These features allow the performance of sensitivity studies in order to investigate the influence of single process parameters or sub-process models on the gasification process. A further reduction in CPU time down to the minute range is feasible, thus the 2Ph-FJM may be applicable for integration into the process control system of a gasifier.

4.2 Experimental validation

In the range z = 30 – 250 mm distance from the burner, simultaneous measurements of droplet size and velocity are performed with phase Doppler anemometry (PDA) at the axis

(r = 0) of the REGA gasifier. In Figure 11, data measured and simulation results from the 2Ph-FJM are shown. The number-averaged mean droplet velocity is already shown in Figure 10. The mean droplet velocity is number-averaged both for simulation and PDA measurement. Close to the nozzle at z < 50 mm, the 2Ph-FJM predicts a rapid acceleration of the droplets. This effect cannot be detected with PDA, since liquid ligaments and non-spherical droplets impede the measurement for z < 50 mm. In the range of 50 mm < z < 150 mm, a plateau of maximum velocity at ~ 42 m/s is measured. Mean droplet velocity simulated with two-phase free jet model is slightly below at a level of ~ 38 m/s but also shows a velocity plateau. Further downstream, velocity decays for both simulation and measured data with a discrepancy of ~ 5 m/s.

Figure 11 also shows Sauter mean diameter of the droplets (SMD) both measured with PDA and simulated with the 2Ph-FJM. The experimental data are derived from radial profile measurements of SMD, the reported values are taken at the centerline of the symmetric profiles. At z < 80 mm on the flame axis, gas temperature is low, thus no significant evaporation takes place. In this area, the local SMD shows a constant value for both simulation and PDA measurement. For z > 80 mm, high gas temperature is present, thus significant droplet evaporation takes place. The local SMD increases with increasing axial distance, since small droplets rapidly evaporate and vanish. Further downstream, SMD decreases again, when the large droplets evaporate to a significant extent, which is beyond the range of the graph. The measured data shows a smooth increase of the SMD whereas the model shows constant droplet diameter close to the nozzle and a rather spontaneous increase at ca. 100 mm. We assume that the effect occur, because no radial transport of droplets is considered in the 2Ph-FJM. However, common tendencies between data from simulation and PDA are apparent.

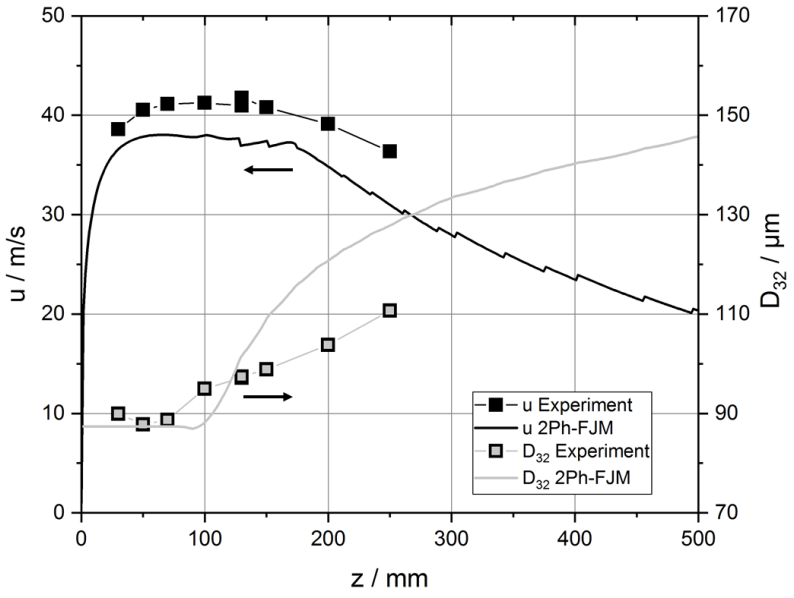

Figure 11: Comparison of number-averaged droplet velocity and the Sauter mean droplet diameter from PDA measurements and the 2Ph-FJM on the jet axis (r = 0)

Figure 12 depicts the gas temperature from the 2Ph-FJM (left), which is already shown in Figure 8 and an OH*-chemiluminescence image (right) from gasification experiment in the REGA gasifier. The OH*-chemiluminescence image is temporally averaged and reverse-Abel-

transformed in post processing. Note that the vertical line along the axis is a numerical artifact from the Abel-transformation. Both images in Figure 12 show the flame structure in the gasifier. High intensity OH*-chemiluminescence indicate zones of high reaction intensity and high temperature (see section 2.4.2). Both images show a cold core in the central area near the nozzle, which is enveloped by the hot reaction zone. Ignition can be observed at the nozzle exit, slightly displaced from the jet axis. The reaction zone forms a fine streak close to the nozzle, which is broadening downstream. On the left side of Figure 12, the rotationally symmetric reaction zone merges on the axis at an axial distance of z = 160 mm. On the right side of Figure 12, no exact axial position can be determined. However, at an axial distance of 150 < z < 170 mm, the most intense OH*-chemiluminescence signal is detected on the axis. Further downstream, the oxygen from the gasification medium is completely consumed, thus reaction intensity decays resulting in a hot plume. Both simulation and PDA measurement show droplets still present at position (see Figure 11). Remaining droplets evaporate in the hot plume and convert to syngas components.

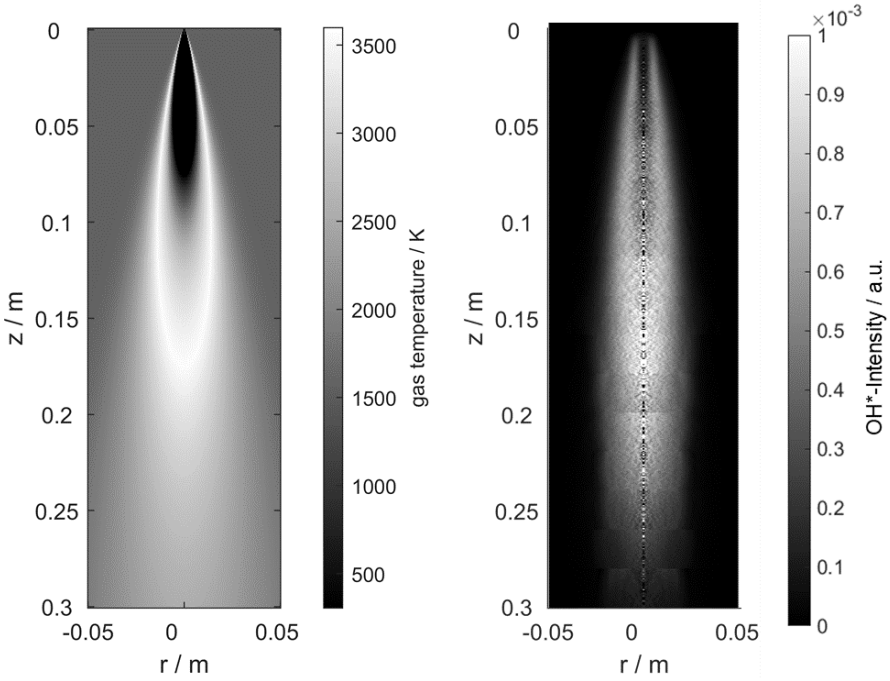

Figure 12: Gas phase temperature simulated with the 2Ph-FJM (left) and an image of OH*-chemiluminescence from the REGA gasifier (right)

5 Summary

A two-phase free jet model (2Ph-FJM) for the simulation of the main reaction zone of an atmospheric entrained flow gasifier is developed in order to perform sensitivity studies on the influence of single model parameters (e.g. burner nozzle dimension, spray droplet size, operating conditions) and sub-process models (e.g. evaporation of fuel droplets) on the gasification process (e.g. flame structure, fuel conversion). The model is a steady-state fluid dynamic model based on a free jet approach from literature. Radial Gaußian profiles of mixing ratio and axial velocity for a single-phase free jet are adapted to the gas phase of the two-phase free jet by a parameter for the exchange of momentum, determined from two-phase

free jet experiments under ambient conditions. With the modified free jet equations, a pattern of axial gas phase velocity and temperature is calculated. Droplets are introduced at the nozzle and transported through the gas phase pattern on straight pathways radially away from the nozzle. Initial droplet size fractions are taken from PDA measurements under ambient conditions. Sub-process models for acceleration, heat-up and evaporation of fuel droplet as well as decomposition of fuel vapor, oxidation reaction and the water gas shift reaction are included. Detailed reaction kinetics, formation of by-products and turbulent structure are not considered in the 2Ph-FJM. Momentum, heat and mass transfer between gas phase and droplets are taken into account.

The 2Ph-FJM presented in this paper is able to calculate the pattern of the main gas components, temperature and fuel conversion in the main reaction zone. Simulation results are approved for a set of experimental data from the bench-scale atmospheric entrained flow gasifier REGA. Droplet velocity and size distribution are measured using phase Doppler anemometry (PDA) and the flame structure is detected using OH*-chemiluminescence imaging. Both PDA measurements and OH*-chemiluminescence images are in good accordance to the simulation results.

The 2Ph-FJM has a modular structure, thus sub-processes models can be changed easily. Compared to RANS or LES simulation, CPU time required for the simulation is several orders of magnitude lower. These features allow the performance of sensitivity studies in order to investigate the influence of single process parameters (e.g. droplet size distribution) or sub-process models (e.g. droplet evaporation) on the entrained flow gasification process.

Acknowledgments

The authors gratefully acknowledge the financial support by the Helmholtz Association of German Research Centers (HGF), within the research program Energy Efficiency, Materials and Resources (EMR). The present work contributes to the Helmholtz Virtual Institute for Gasification Technology - HVIGasTech (VH-VI-429, http: //www.hvigastech.org/).

References

[1] Fleck S., Santo U., Hotz C., Jakobs T., Eckel G., Mancini M., Weber R., Kolb T. Entrained flow gasification Part 1: Gasification of glycol in an atmospheric-pressure experimental rig. Fuel 2018;217:306–19. doi:10.1016/j.fuel.2017.12.077.

[2] Mancini M., Alberti M., Dammann M., Santo U., Eckel G., Kolb T., Weber R. Entrained flow gasification. Part 2: Mathematical modeling of the gasifier using RANS method. Fuel 2018;225(4):596–611. doi:10.1016/j.fuel.2018.03.100.

[3] Eckel G., Le Clercq P., Kathrotia T., Saenger A., Fleck S., Mancini M., Kolb T., Aigner M. Entrained flow gasification. Part 3: Insight into the injector near-field by Large Eddy Simulation with detailed chemistry. Fuel 2018;223:164–78. doi:10.1016/j.fuel.2018.02.176.

[4] Ricou F.P. Measurement of entrainment by turbulent jets [Dissertation]. London: University of London; 1960.

[5] Jakobs T., Djordjevic N., Fleck S., Mancini M., Weber R., Kolb T. Gasification of high viscous slurry R&D on atomization and numerical simulation. Applied Energy 2012;93:449–56. doi:10.1016/j.apenergy.2011.12.026.

[6] Ruden P. Turbulente Ausbreitungsvorgänge im Freistrahl. Naturwissenschaften 1933;21(21-23):375–8. doi:10.1007/BF01451791.
[7] Reichardt H. Gesetzmäßigkeiten der freien Turbulenz. VDI Forschungsheft 1951(414):2–30.
[8] George W.K. The Self-Preservation of Turbulent Flows and Its Relation to Initial Conditions and Coherent Structures 1989.
[9] Becker H.A., Hottel H.C., Williams G.C. The nozzle-fluid concentration field of the round, turbulent, free jet. J. Fluid Mech. 1967;30(02):285. doi:10.1017/S0022112067001430.
[10] Dahm W.J.A. Experiments on entrainment, mixing and chemical reactions in turbulent jets at large Schmidt number [Dissertation]. Pasadena: California Institute of Technology; 1985.
[11] Dowling D.R., Dimotakis P.E. Similarity of the concentration field of gas-phase turbulent jets. Journal of Fluid Mechanics 1990(218):109–41.
[12] Panchapakesan N.R., Lumley J.L. Turbulence measurements in axisymmetric jets of air and helium. Part 1. Air jet. Journal of Fluid Mechanics 1993;246:197–223. doi:10.1017/S0022112093000096.
[13] Hussein H.J., Capp S.P., George W.K. Velocity measurements in a high-Reynolds-number, momentum-conserving, axisymmetric, turbulent jet. J. Fluid Mech. 1994;258(-1):31. doi:10.1017/S002211209400323X.
[14] Hinze JO. Turbulence. 2nd ed. New York, NY: McGraw-Hill; 1975.
[15] Richards C.D., Pitts W.M. Global density effects on the self-preservation behaviour of turbulente jets. J. Fluid Mech. 1993(254):417–35.
[16] Mi J., Nobes D.S., Nathan G.J. Influence of jet exit conditions on the passive scalar field of an axisymmetric free jet. Journal of Fluid Mechanics 2001(432):91–125.
[17] Xu G., Antonia R. Effect of different initial conditions on a turbulent round free jet. Exp Fluids 2002;33(5):677–83. doi:10.1007/s00348-002-0523-7.
[18] Ricou F.P., Spalding D.B. Measurements of entrainment by axisymmetrical turbulent jets. J. Fluid Mech. 1961;11(1):21–32. doi:10.1017/S0022112061000834.
[19] Rotta JC. Turbulente Strömungen: Eine Einführung in die Theorie und ihre Anwendung. Göttingen, Göttingen: Niedersächsische Staats-und Universitätsbibliothek; Univ.-Verl. Göttingen; 2010.
[20] Corrsin S. Investigation of flow in an axially symmetrical heated jet of air 1943.
[21] Reichardt H. Impuls- und Wärmeaustausch in freier Turbulenz 1944.
[22] Hinze J.O., Van Der Hegge Zijnen B.G. Transfer of heat and matter in the turbulent mixing zone of an axially symmetrical jet. Appl. Sci. Res. 1949.
[23] Alexander L.G., Baron T., Comings E.W. Transport of momentum, mass, and heat in turbulent jets. University of Illinois Bulletin Series 1953(413).
[24] Wygnanski I., Fiedler H. Some measurements in the self-preserving jet. J. Fluid Mech. 1969;38(03):577. doi:10.1017/S0022112069000358.
[25] Günther R. Verbrennung und Feuerungen. Berlin, Heidelberg: Springer Berlin Heidelberg; 1974.
[26] Kremer H. Zur Ausbreitung inhomogener turbulenter Freistrahlen und turbulenter Diffusionsflammen [Dissertation]. Karlsruhe: Universiät Karlsruhe (TH); 1964.
[27] Fast G. Laseroptische Strömungsdiagnostik zu Selbstzündungsprozessen bei Freistrahlen [Dissertation]. Eggenstein-Leopoldshafen: Forschungszentrum Karlsruhe; 2007.
[28] Thring M.W., Newby M.P. Combustion length of encloed turbulent jet flames. Symposium (International) on Combustion 1953;4:789–96.

[29] Galeazzo F.C.C. Simulation of Turbulent Flows with and without Combustion with Emphasis on the Impact of Coherent Structures on the Turbulent Mixing [Dissertation]: Karlsruher Institut für Technologie; 2013.
[30] Townsend AA. The structure of turbulent shear flow. 2nd ed. Cambridge: Cambridge Univ. Press; 1976.
[31] Lockwood F.C., Moneib H.A. Fluctuating Temperature Measurements in a Heated Round Free Jet. Combustion Science and Technology 1980;22(1-2):63–81. doi:10.1080/00102208008952372.
[32] Chen CJ, Rodi W. A Review of experimental data of vertical turbulent buoyant jets; 1975.
[33] Hetsroni G. Particles-Turbulence Interaction. International Journal of Multiphase Flow 1989(15):735–46.
[34] Crowe CT, Oweis GF, Ceccio SL, Matsumoto Y, Tropea C, Roisman IV. Multiphase Flow Handbook. CRC Press; 2005.
[35] Subramanian V., Ganesh R. Influence of free stream velocity on the entrainment by single- and two-phase axisymmetric jets. AIChE J. 1984;30(6):1010–3. doi:10.1002/aic.690300626.
[36] Melville W.K., Bray K.N.C. The Two-Phase Turbulent Jet. International Journal of Heat and Mass Transfer 1979(22):279–87.
[37] Lau T.C.W., Nathan G.J. The effect of Stokes number on particle velocity and concentration distributions in a well-characterised, turbulent, co-flowing two-phase jet. J. Fluid Mech. 2016;809:72–110. doi:10.1017/jfm.2016.666.
[38] Smith M.S. The Effect of buoyancy in Enclosed Turbulent Flames [Dissertation]. Surrey: University of Surrey; 1976.
[39] Curtet R. Confined Jets and Recirculation Phenomena with cold air. Combustion and Flame 1958(2):83–411.
[40] Craya A., Curtet R. Sur l'evolution d'un jet en espace confine 1955.
[41] Becker H.A., Hottel H.C., Williams G.C. Mixing and Flow in ducted turbulent Jets: At Cornell University Ithaca, New York, August 27 to September 1, 1962 1963.
[42] Field MA. Combustion of pulverized coal. Leatherhead (Sy.); 1967.
[43] Guruz A.G., Guruz H.K., Osuwan S., Steward F.R. Aerodynamics of a Confined Burning Jet. Combustion Science and Technology 1974;9(3-4):103–10. doi:10.1080/00102207408960344.
[44] Stephan P, Mewes D, Kabelac S, Kind M, Schaber K, Wetzel T (eds.). VDI-Wärmeatlas. Wiesbaden: Springer; 2017.
[45] Morsi S.A., Alexander A.J. An investigation of particle trajectories in two-phase flow systems. J. Fluid Mech. 1972;55(02):193. doi:10.1017/S0022112072001806.
[46] Sazhin S. Droplets and Sprays. London: Springer London; 2014.
[47] Ranz W.E., Marshall W.R.J. Evaporation from Drops: Part I. Chemical Engineering Progress 1952(Vol. 48, No. 3).
[48] Higman C, van Burgt Md. Gasification. 2nd ed. Amsterdam: Gulf Professional Pub./Elsevier Science; 2008.
[49] Sänger A.D. Zerstäubung hochviskoser Fluide bei variierendem Systemdruck - Grundlagenforschung zur Hochdruck-Flugstromvergasung. Dissertation 2018. doi:10.5445/IR/1000087397.
[50] Wachter S., Jakobs T., Kolb T. Experimental investigation on the influence of system pressure on resulting spray quality and jet breakup applying pressure adapted twin-fluid

nozzles. International Journal of Multiphase Flow 2020;125:103189. doi:10.1016/j.ijmultiphaseflow.2019.103189.
[51] García-Armingol T., Ballester J. Influence of fuel composition on chemiluminescence emission in premixed flames of CH 4 /CO 2 /H 2 /CO blends. International Journal of Hydrogen Energy 2014;39(35):20255–65. doi:10.1016/j.ijhydene.2014.10.039.
[52] Kopp M., Brower M., Mathieu O., Petersen E., Güthe F. CO2* chemiluminescence study at low and elevated pressures. Appl. Phys. B 2012;107(3):529–38. doi:10.1007/s00340-012-5051-4.
[53] Nori V., Seitzman J. Chemiluminescence Measurements and Modeling in Syngas, Methane and Jet-A Fueled Combustors 2007. doi:10.2514/6.2007-466.
[54] Lauer M., Sattelmayer T. On the adequacy of chemiluminescence as a measure for heat release in turbulent flames with mixture gradients. Journal of Engineering for Gas Turbines and Power 2010;132(6):61502.
[55] Lauer M. Determination of the Heat Release Distribution in Turbulent Flames by Chemiluminescence Imaging [Dissertation]. München: TU München; 2011.
[56] Lauer M., Sattelmayer T. Heat Release Calculation in a Turbulent Swirl Flame from Laser and Chemiluminescence Measurements. 14th Int Symp on Applications of Laser Techniques to Fluid Mechanics 2008.
[57] Birch A.D., Brown D.R., Dodson M.G., SWAFFIELD F. The Structure and Concentration Decay of High Pressure Jets of Natural Gas. Combustion Science and Technology 1984;36(5-6):249–61. doi:10.1080/00102208408923739.
[58] Brown B., Smoot L.D., Smith P.J., Hedman P.O. Measurement and prediction of entrained-flow gasification processes. AlChE Journal 1988;34(3):435–46.
[59] Chigier NA, Farago Z. Atomization and Sprays: Morphological classification of disintegration of round liquid jets in a coaxial air stream; 1992.
[60] Matas J.-P., Delon A., Cartellier A. Shear instability of an axisymmetric air–water coaxial jet. J. Fluid Mech. 2018;843:575–600. doi:10.1017/jfm.2018.167.